# Tuning electronic and composition effects in ruthenium-copper alloy nanoparticles anchored on carbon nanofibers for rechargeable Li-$CO_2$ batteries

Jin, Yachao; Chen, Fuyi; Wang, Jiali; Johnston, Roy L.

*DOI:*
10.1016/j.cej.2019.121978



*Document Version*
Peer reviewed version

*Citation for published version (Harvard):*
Jin, Y, Chen, F, Wang, J & Johnston, RL 2019, 'Tuning electronic and composition effects in ruthenium-copper alloy nanoparticles anchored on carbon nanofibers for rechargeable Li-$CO_2$ batteries', *Chemical Engineering Journal*, vol. 375, 121978. https://doi.org/10.1016/j.cej.2019.121978

# Tuning Electronic and Composition Effects in Ruthenium-Copper alloy Nanoparticles Anchored on Carbon Nanofibers for Rechargeable Li-$CO_2$ Batteries

Yachao Jin,[†] Fuyi Chen*[,†] , Jiali Wang*[,†] and Roy L. Johnston[#]

[†]State Key Laboratory of Solidification Processing, Northwestern Polytechnical University; Xi'an, 710072, China.

[#]School of Chemistry, University of Birmingham, Birmingham B15 2TT, UK

[*] Corresponding author: Tel./Fax: +86 029-88492052. E-mail: fuyichen@nwpu.edu.cn (Fuyi Chen), jialiwang@mail.nwpu.edu.cn (Jiali Wang)

## ABSTRACT

Rechargeable Li-$CO_2$ batteries are attracting increasing attention due to their high energy density and ability to capture greenhouse gas $CO_2$. However, the difficulty in decomposing electronically insulating and electrochemically sluggish $Li_2CO_3$ discharge products under low charge voltages is still a major challenge. Herein, for the first time, a composite of intermixed ruthenium-copper alloy nanoparticles uniformly anchored on carbon nanofibers (*i*-RuCu/CNFs) as efficient cathode electrocatalysts for Li-$CO_2$ batteries is well designed. Remarkably, the Li-$CO_2$ batteries with *i*-$Ru_4Cu_1$/CNFs cathodes can be steadily cycled for over 110 cycles without capacity decay. And they show record-high rate capability along with much decreased overpotentials of 1.45 and 1.56 V even at current densities of 1000 and 2000 mA $g^{-1}$, respectively. Moreover, a high discharge capacity of 15753 mAh $g^{-1}$ is obtained for Li-$CO_2$ batteries based on *i*-$Ru_4Cu_1$/CNFs, and 99.3% of discharged capacity could be reversibly charged, giving the significant Coulombic efficiency. This work demonstrates the powerfully catalytic activity of intermixed RuCu nanoalloys for easily decomposing discharge

products in Li-$CO_2$ batteries and provides more insights to design more highly efficient cathode electrocatalysts for Li-$CO_2$ batteries and beyond.

***Keywords:*** Li-$CO_2$ battery; intermixed RuCu nanoalloy; ultralow overpotential; superb rate capability

## 1. Introduction

Conversion of carbon dioxide ($CO_2$) to renewable energies in an environmental-friendly way has been considered as an appealing and essential approach for mitigating climate change and achieving sustainable development [1-3]. In recent decades, various routes have been investigated and employed to fulfill this purpose [4-7]. Li-$CO_2$ batteries represent one kinds of novel and innovational technique that could coinstantaneously capture and convert $CO_2$ to electricity, differing from traditionally electrochemical reduction methods [8-11]. According to early researches, the work principle of Li-$CO_2$ batteries was proposed to comply with reversibly electrochemical reaction of $4Li + 3CO_2 \leftrightarrow 2Li_2CO_3 + C$, which could theoretically deliver a high energy density of 1876 Wh $kg^{-1}$ [12, 13]. However, $Li_2CO_3$, as the main discharge product, is much thermodynamically stable, electronically insulating and electrochemically sluggish [14-16]. As a result, the difficulty of completely electrochemical decomposition of $Li_2CO_3$ within a low potential during the charge process seriously lowers energy efficiency and hinders deployment of Li-$CO_2$ batteries [17].

Electrocatalysts utilized to facilitate the kinetics of discharge and charge processes in Li-$CO_2$ batteries have been extensively studied [18], such as carbon nanomaterials [19, 20], transition metals [12, 15, 21-24], metal oxides [25, 26], metal carbides [27, 28] and redox mediator [29]. Zhang and co-workers introduced carbon nanotubes as cathode catalyst in rechargeable Li-$CO_2$ batteries [30], which showed a discharge capacity of 5786 mAh $g^{-1}$ and cycling performance of 20 cycles at current density of 100 mA $g^{-1}$. Ma et al. designed porous $Mn_2O_3$ cathode for Li-$CO_2$ batteries that delivered decreased discharge/charge voltage gap of

1.4 V at a current density of 50 mA $g^{-1}$ [25]. By comparison with carbon and metal oxide nanomaterials, trasition metals as cathode catalyst usually exhibit better catalytic activity in Li-$CO_2$ batteries [31]. For example, Zhou's group reported that the reversible Li-$CO_2$ batteries with Ru@Super P as cathode showed excellent performance [12], which demonstrated a discharge capacity as high as 8229 mAh $g^{-1}$ and was discharged and charged for 80 cycles at current density of 100 mA $g^{-1}$. They elucidated that Ru is capable of promoting the reaction between $Li_2CO_3$ and C, optimizing charge route and lowering charge voltage compared to the pathway through self-decomposition of $Li_2CO_3$ [32]. Nevertheless, the pure monometallic Ru as cathode electrocatalyst displays very limited ability for catalyzing interactions between $Li_2CO_3$ and C for lack of promoting factors, such as geometric, compositional and electronic effects.

Currently, incorporating a second metal provides promising approach to energetically improve the catalytic activity over its monometallic analogue owing to the synergistic effects between two metals [33, 34], which has been considerably used in fields of catalysis [35], sensing [36] as well as Li-$O_2$ batteries [37]. Lu et al. designed PtAu/C bimetallic nanoparticles as bifunctional catalyst in Li-$O_2$ batteries [38], showing enhanced round-trip efficiency. They proposed that surface Au and Pt atoms are primarily responsible for ORR and OER kinetics in Li-$O_2$ batteries, respectively. Song and co-workers prepared PdCu bimetallic nanoparticles with mixed disordered fcc and ordered B2-type phases [39]. The resulting PdCu catalyst demonstrated superb round-trip efficiency of ~80% and cyclic stability for Li-$O_2$ batteries, which is ascribed to the weak $LiO_2$ adsorption strength caused by electron transfer from Cu to top-layer Pd atoms on the surface. More recently, the phase separated Ru-Cu nanoparticles on graphene was reported by Zhang et al. for improving Li-$CO_2$ battery performance [40]. Benefitting from synergistic effect between individual Ru and Cu nanoparticles, the Li-$CO_2$ batteries exhibited low overpotential and long cycle life. However, one can see that the Ru-Cu nanoparticles are not in the form of alloys. It is well-

known that solid solution phase of bimetallic alloy catalyst is usually more favorable to achieve the completely synergistic effects between two metal elements [41, 42]. So far, rare studies on catalytic decomposition of $Li_2CO_3$ using RuCu nanoalloys has been reported. Therefore, designing a intermixed RuCu nanoalloy cathode catalyst is highly desired to further greatly improve the performance for Li-$CO_2$ batteries.

Herein, we successfully designed and synthesized the intermixed ruthenium-copper single-phase solid solution nanoparticles that uniformly dispersed on carbon nanofibers (denoted as *i*-RuCu/CNFs) via a facile and effective solvothermal method although Ru and Cu are thermodynamically immiscible. Benefiting from the advantageous compositional and electronic effects between Ru and Cu, the Li-$CO_2$ batteries with *i*-RuCu/CNFs composite as cathodic electrocatalyst exhibit remarkably enhanced kinetics for $CO_2$ reduction and evolution. Our results show that the fabricated Li-$CO_2$ battery based on *i*-$Ru_4Cu_1$/CNFs electrocatalyst demonstrates markedly low overpotentials of 1.45 and 1.56 V even at the current densities of 1000 and 2000 mA $g^{-1}$, respectively. What is more, such Li-$CO_2$ batteries can be steadily discharged-charged over 110 cycles at a large current density of 500 mA $g^{-1}$ without the capacity decay. Notably, compared with the previously reported Ru-Cu nanoparticles with separated phase, the *i*-$Ru_4Cu_1$/CNFs electrocatalyst shows more improved electrocatalytic performance for Li-$CO_2$ batteries. This work demonstrates the powerfully catalytic activity of intermixed RuCu nanoalloys for easily decomposing discharge products in Li-$CO_2$ batteries and provides more insights to design more highly efficient cathode electrocatalysts for Li-$CO_2$ batteries and beyond

## 2. Experimental Section

### *2.1 Chemicals*

All chemical reagents used in experiments were analytical grade without any additional purification. Ruthenium chloride hydrate ($RuCl_3 \cdot nH_2O$), copper chloride dihydrate

($CuCl_2 \cdot 2H_2O$), ethylene glycol (EG), concentrated sulfuric acid ($H_2SO_4$), hydrochloric acid (HCl), potassium permanganate ($KMnO_4$), hydrogen peroxide ($H_2O_2$), sodium nitrate ($NaNO_3$) were bought from Sinopharm Chemical Reagent Co. Ltd. Lithium bis (trifluoromethane sulfonimide) (LiTFSI, 99.95%), Dimethylsulfoxide (DMSO, anhydrous, 99.9%) and carbon nanofibers (CNFs) were bought from Sigma-Aldrich. The Whatman separator was bought from GE Healthcare Life Sciences. Carbon paper was bought from the Fuel Cell Store. Ultrapure water with the resistance of 18.25 MΩ cm was used in this experiment.

*2.2 Synthesis of the intermixed RuCu/CNFs nanoalloy electrocatalysts*

The CNFs were firstly oxidized according to a modified Hummers method [43, 44]. Then, the oxidized CNFs were taken as substrates to synthesize the intermixed RuCu nanoalloys through the solvothermal method. Taking *i*-$Ru_4Cu_1$/CNFs composite as the sample, the oxidized CNFs (50 mg) was mixed with EG (50 mL) containing $RuCl_3 \cdot nH_2O$ (8 mM) and $CuCl \cdot 2H_2O$ (2 mM) in a 100 mL baker to form a homogeneous solution under the help of ultrasonication. Subsequently, this solution was allowed to stir overnight. The total precursor concentration is a constant value of 10 mM. Then, the resulting solution was transferred to a 100 mL Teflon-lined autoclave and heated at 180 °C for 10 h. After natural cooling down to room temperature, the black precipitates were collected and washed by ethanol and ultrapure water several times, and dried via the freeze-dried process overnight. The obtained products were further heat treated under the argon gas at 350 °C for 2h for the final *i*-$Ru_4Cu_1$/CNFs nanomaterials. Accordingly, the other electrocatalysts including *i*-$Ru_5Cu_1$/CNFs, *i*-$Ru_3Cu_1$/CNFs, *i*-$Ru_1Cu_1$/CNFs, Ru/CNFs and Cu/CNFs were prepared by using the same method with only changing the metal precursor concentration. The $Ru_xCu_y$ was assigned based on the precursor ratio of $RuCl_3 \cdot nH_2O$ and $CuCl_2 \cdot 2H_2O$. The carbon-free *i*-$Ru_4Cu_1$ nanomaterials were prepared by using the same method as that of preparing *i*-

$Ru_4Cu_1$/CNFs nanomaterials only without the addition of CNFs substrates, which were subsequently coated on the Ni foam with a layer of Au film for the carbon-free cathode electrodes.

Furthermore, the nanomaterials that Ru and Cu nanoparticles separately dispersed on CNFs with separated phase (referred to as *s*-$Ru_4$-$Cu_1$/CNFs hereafter) were also prepared based on the method of preparing *i*-$Ru_4Cu_1$/CNFs with modification. Briefly, the oxidized CNFs (50 mg) was mixed with EG (50 mL) containing the $RuCl_3 \cdot nH_2O$ (8 mM). Then the resulting homogeneous solution was heated at 180 °C for 10 h in a 100 mL Teflon-lined autoclave. After cooling down, the precipitates were collected and washed by ethanol and ultrapure water several times, and were then re-dispersed into the EG (50 mL) containing $CuCl_2 \cdot 2H_2O$ (2 mM). Subsequently, the resulting solution was allowed to stir overnight and transferred to a 100 mL Teflon-lined autoclave for reaction at 180 °C for 10 h. After cooling down, the precipitates were collected and washed, and dried via the freeze-dried process overnight. The obtained products were further heat treated under the argon gas at 350 °C for 2h for the final *s*-$Ru_4$-$Cu_1$/CNFs nanomaterials.

*2.3 Physical characterization*

Transmission electron microscope (TEM) and High-resolution TEM (HRTEM) images were obtained with a FEI Talos F200X (USA) operated at 200 kV. High-angle annular dark-field scanning transmission electron microscope (HAADF-STEM) images and elemental mappings were recorded using TEM coupled with energy-dispersive X-ray spectroscope (EDS). Scanning electron microscope (SEM) images were obtained on a FEI Helious G4 CX (USA). X-ray diffraction (XRD) patterns were performed on a PANalytical X'Pert Pro MPD with Cu Kα radiation (λ = 1.5406 Å). The accelerating voltage and current employed were 40 kV and 40 mA, respectively. The compositional ratio were determined by inductively coupled plasma-mass spectrometry (ICP-MS, NexION 350D) and X-Ray fluorescence spectroscopy

(XRF, Bruker S8 Tiger). X-ray photoelectron spectroscope (XPS) was carried out with an ESCALAB 250 instrument under the ultrahigh vacuum of 10−9 Torr using monochromated Al Kα radiation (hν = 1486.6 eV), all binding energies were calibrated by the carbon peak (C 1s) at about 284.5 eV. The Fourier transform infrared spectra (FTIR, Bruker vertex 80) were performed to analyse the discharge/charge processes. The Raman spectra (WITec, Alpha300R) and gas chromatography (GC, Techcomp, GC7900) were taken to study the discharge products and gas emission during the cycling process. The discharged/charged cathode electrodes were washed three times by dimethylsulfoxide (DMSO) to remove the residue Bis(trifluoromethane)sulfonimide (LiTFSI) salt before the characterization of XRD, SEM, TEM, XPS, FTIR and Raman. The mass of metal was determined by thermogravimetric analysis (TGA) measurements (Netzsch).

*2.4 Assembly of Batteries and measurements*

The cathodic electrodes of Li-$CO_2$ batteries were prepared via a slurry. Typically, 5 mg of obtained electrocatalyst with 10% PVDF binder were dispersed in 1mL of the N-methyl pyrrolidone (NMP) to form a homogeneous slurry under the help of ultrasonication. Then, such slurry was coated on a carbon paper (10 mm in diameter) with the loading amount of 0.2 mg as the cathodic electrode. The obtained cathodic electrodes were further dried at 80 °C overnight under vacuum. The lithium-metal chips (diameter:15.6 mm, thickness: 0.25 mm) and the glass fiber separator (Whatman, diameter: 19 mm) were used as the anodic electrode and separator, respectively. The electrolyte used in this research is 1 M LiTFSI dissolved in the DMSO solution. Finally, the 2032 coin-type cells with the holes on the cathode side were taken to fabricate the Li-$CO_2$ batteries in a glovebox filled with high-purity argon gas. The as-prepared coin cells were sealed into the home-made chamber filled with pure $CO_2$. On the other hand, the Li-$O_2$/air batteries were prepared same as that of Li-$CO_2$ batteries, which were sealed into the home-made chamber filled with pure $O_2$ or dry air, respectively. To monitor the gas emission of Li-$CO_2$ batteries during the charge process, the customized Swagelok-type

Li-$CO_2$ batteries were also fabricated. The Li-$CO_2$ battery properties were measured in a LAND cycler (Wuhan Land Electronic Co. Ltd). The capacity values were normalized by the mass of electrocatalyst in cathodic cathodes. The overpotentials of Li-$CO_2$ batteries were calculated by voltages difference at the middle of the charge/discharge plateaus.

## 3. Results and discussion

*3.1 Physcial characterization of i-$Ru_4Cu_1$/CNFs*

The phase structures of resulting nanomaterials were initially examined by X-ray diffraction (XRD) pattern. As illustrated in Fig. 1a, the typical Bragg peaks attributing to hexagonal Ru are clearly observed for both *i*-$Ru_4Cu_1$/CNFs and Ru/CNFs [45, 46], with the peak at 25° associated to the (002) diffraction peak of CNFs substrates. Compared with the XRD pattern of Cu/CNFs (Fig. S1), one can see no other additional peaks for Cu in *i*-$Ru_4Cu_1$/CNFs. Moreover, the diffraction peaks of *i*-$Ru_4Cu_1$/CNFs shifted to higher angles compared to those of Ru/CNFs, which can be ascribed to the incorporation of Cu atoms into the Ru crystal lattice without changing the crystal structure and an indicative of formation of hexagonal close-packed (hcp) *i*-$Ru_4Cu_1$ nanoalloy [47, 48]. The scanning electron microscopy (SEM) and transmission electron microscopy (TEM) techniques were performed to investigate the morphologies and nanostructures of *i*-$Ru_4Cu_1$/CNFs (Fig. S2 and Fig. 1b, c). Obviously, sphere-shaped *i*-$Ru_4Cu_1$ nanoalloys with diameters ranging from 5 to 15 nm are uniformly distributed on the CNFs surfaces. High-resolution TEM (HRTEM) image shown in Fig. 1d displays the continuous lattice fringes, indicating the highly crystalline nature of *i*-$Ru_4Cu_1$ nanoalloys. The confirmed lattice fringe distance of 0.226 nm (Fig. 1e and Fig. S3c) are ascribed to the (100) plane of *i*-$Ru_4Cu_1$ nanoalloy [45, 47], which reveals a lattice contraction compared to that of pure Ru owing to the formation of *i*-$Ru_4Cu_1$ nanoalloy, consistent well with the XRD result. The high-angle annular dark-field scanning TEM (HAADF-STEM) image in conjunction with energy-dispersive X-ray spectroscopy (EDS)

profile illustrate that Ru and Cu elements are distributed evenly in each nanoparticle (Fig. 1g-i, Fig. S4). The EDS line-scan profile recorded in a single nanoparticle further verifies the formation of homogeneous *i*-$Ru_4Cu_1$ nanoalloys (Fig. 1j). To precisely determine the atomic compositions of Ru and Cu in *i*-$Ru_4Cu_1$ nanoalloy, the inductively coupled plasma-mass spectrometry (ICP-MS) and X-Ray fluorescence spectroscopy (XRF) as well as EDS were conducted [49, 50]. The atomic percentage of Ru and Cu were measured to be 80.2% Ru and 19.8% Cu in *i*-$Ru_4Cu_1$ nanoalloy (Table S1 and Fig. S5), respectively, which is in good accordance with the feeding ratio of precursor solution. Furthermore, the mass proportion of *i*-$Ru_4Cu_1$ nanoalloy and CNFs substrate in *i*-$Ru_4Cu_1$/CNFs nanomaterial measured by thermogravimetric analysis (TGA) are 38.3% and 61.7%, respectively (Fig. S6).

X-ray photoelectron spectroscopy (XPS) analysis was employed to investigate the chemical valences and electronic interactions of Ru and Cu in *i*-$Ru_4Cu_1$/CNFs. As shown in Fig. 2a, the survey spectrum of *i*-$Ru_4Cu_1$/CNFs exhibits the clear characteristic peaks for Ru and Cu, and the atomic percentage of Ru and Cu on catalyst surface was determined to be 82.2 and 17.8, respectively. Combined with the consistent ICP-MS results, it is concluded that Ru and Cu are uniformly distributed in both bulk and surface, confirming the homogeneous *i*-$Ru_4Cu_1$ nanoalloys. As determined by the high-resolution XPS spectra of Ru (Fig. 2b and Fig. S7), the binding energy of 461.4 (Ru $3p_{3/2}$) and 483.6 eV (Ru$3p_{1/2}$) are attributed to $Ru^0$, while the binding energy of 464.2 (Ru$3p_{3/2}$) and 484.2 eV (Ru$3p_{1/2}$) are assigned to the presence of $Ru^{4+}$ [51-53], emphasizing that Ru in *i*-$Ru_4Cu_1$/CNFs are mainly present in metallic state. More importantly, it is noted from Fig. 2b that the XPS core-level spectra of Ru 3*p* in *i*-$Ru_4Cu_1$/CNFs displays a negative shift with respect to those of Ru/CNFs, indicating charge transfer from Cu to Ru due to the higher electronegativity of Ru [54], which can be further confirmed by the positive shift of core-level spectra of Cu 2*p* in *i*-$Ru_4Cu_1$/CNFs compared with that in Cu/CNFs (Fig. 2c). The bingding energy located at 952.4 (Cu $2p_{1/2}$) and 932.6 eV (Cu $2p_{3/2}$) are indicative of $Cu^0$, whereas the peaks centered at 953.8 (Cu $2p_{1/2}$) and 934 eV

(Cu $2p_{3/2}$) are attributed to $Cu^{2+}$ in *i*-$Ru_4Cu_1$/CNFs [55, 56]. One can see that the complete alloying between Ru and Cu effectively reduces the Cu oxidation, which is favorable for electrocatalytic process. Moreover, as shown in Fig. S8, with increasing Cu contents in *i*-RuCu/CNFs, the binding energy of Ru 3*p* was observed to continuously shift to lower values, demonstrating the gradual alloying and robust electronic interactions between Ru and Cu. To prove this phenomenon, the valence band spectra (VBS) was futher performed to study the electronic structure. Fig. 2d exhibits an effective downshift of the d-band center in *i*-$Ru_4Cu_1$/CNFs relative to that of pure Ru/CNFs. Such advantageous modification of electronic structure indicates the promising potential of *i*-$Ru_4Cu_1$/CNFs for greatly improved catalytic activities [57].

*3.2 Performance of Li-$CO_2$ battery based on i-$Ru_4Cu_1$/CNFs electrocatalyst*

Then, we systematically evaluated the electrochemical performance of *i*-$Ru_4Cu_1$/CNFs as cathodes for Li-$CO_2$ batteries. As shown in Fig. 3a, the Li-$CO_2$ battery based on *i*-$Ru_4Cu_1$/CNFs shows the lowest charge-discharge overpotential of 0.9 V coupling with reduced charge voltage of 3.7 V at a constant current density of 100 mA $g^{-1}$. However, the Li-$CO_2$ batteries with Ru/CNFs, Cu/CNFs and CNFs as cathode electrocatalysts display much higher charge-discharge overpotentials (1.32, 1.46 and 1.59 V, respectively) and charge voltages (4.03, 4.14 and 4.22 V, respectively) (Fig. 3b, Fig. S9 and Fig. S10). These results indicate that the battery performance obtained by *i*-$Ru_4Cu_1$/CNFs cathode is remarkably improved by alloying Ru with Cu, even much superior to that of Li-$CO_2$ batteries based on phase separated Ru-Cu nanoparticles and most previously reported Li-$CO_2$ batteries (Table S2) [15, 21, 22, 25]. Besides, the various *i*-RuCu/CNFs nanomaterials with different Ru and Cu atomic ratios have also been prepared and used to fabricate corresponding Li-$CO_2$ batteries. As shown in Fig. S11, with the gradual increase of Cu contents in various *i*-RuCu/CNFs electrocatalysts, the properties of their Li-$CO_2$ batteries have been

correspondingly changed. Attractively, the Li-$CO_2$ battery based on *i*-$Ru_4Cu_1$/CNFs electrocatalyst demonstrates the lowest charge-discharge overpotential, revealing that the kinetics of discharge and charge processes in Li-$CO_2$ batteries are successfully accelerated by the bimetallic *i*-$Ru_4Cu_1$/CNFs naoalloys with the optimized Ru/Cu atomic ratio. Therefore, the *i*-$Ru_4Cu_1$/CNFs electrocatalyst is chosen for the further research. Recent researches have demonstrated that Ru is an excellent candidate for promoting interaction between $Li_2CO_3$ and C during charge process through the reversibly electrochemical reaction of $2Li_2CO_3 + C \leftrightarrow 4Li + 3CO_2$ [12], which is a highly favorable pathway to particularly decrease charge voltage of Li-$CO_2$ batteries. In this work, the bimetallic *i*-$Ru_4Cu_1$/CNFs nanoalloy possesses the effectively modified electronic structure, as manifested in the downshift of d-band center, resulting in a favorable binding of $Li_2CO_3$ [54, 57], which is more beneficial for accelerating reaction between $Li_2CO_3$ and C [40]. Therefore, the reaction kinetics of $Li_2CO_3$ formation and decomposition are further facilitated by the bimetallic *i*-$Ru_4Cu_1$/CNFs. Whereas, such effect is not obtained for Li-$CO_2$ batteries with monometallic Ru/CNFs and Cu/CNFs electrocatalysts.

Furthermore, in practical Li-air batteries, $Li_2CO_3$ is still one of the major by-products that deteriorates battery properties, causing high charge voltage and poor cyclability [58]. Hence, to achieve high performance of practical Li-air batteries, it is essential to decrease the decomposition voltage of $Li_2CO_3$. Fortunately, the bimetallic *i*-$Ru_4Cu_1$/CNFs prepared in this work has demonstrated excellent capability to decompose $Li_2CO_3$ at low charge voltage in Li-$CO_2$ batteries. By using *i*-$Ru_4Cu_1$/CNFs as cathodic electrocatalyst, the Li-air batteries shows not only the enhanced discharge voltage of 2.94 V but also the decreased charge voltage, as for the Li-$CO_2$ batteries based on *i*-$Ru_4Cu_1$/CNFs (Fig. 3c and Fig. S12), indicating the effectiveness of the bimetallic *i*-$Ru_4Cu_1$/CNFs for improving the performance of Li-air batteries. In addition, the *i*-$Ru_4Cu_1$/CNFs was further subjected to test the long-term stability of Li-$CO_2$ battery cycled at a current density of 500 mA $g^{-1}$ with limited capacity of 1000 mAh $g^{-1}$. As shown in Fig. 3d, it is noteworthy that Li-$CO_2$ battery based on *i*-$Ru_4Cu_1$/CNFs

displays a superb cycling performance for more than 110 cycles with much high discharge voltages (Fig. 3e), in a sharp contrast, Li-$CO_2$ battery based on Ru/CNFs can only survive to 43 cycle at the identical condition. The time-voltage curves also clearly confirms that the Li-$CO_2$ battery based on *i*-$Ru_4Cu_1$/CNFs illustrates more stable cyclability with dramatically increased discharge and decreased charge voltages than that based on Ru/CNFs (Fig. 3f). Moreover, the cycling performance of the Li-$CO_2$ batteries based on various *i*-RuCu/CNFs electrocatalysts with different atomic ratios were also systematically examined. As illustrated in Fig. S13, the Li-$CO_2$ battery based on *i*-$Ru_4Cu_1$/CNFs electrocatalyst reveals the most excellent cycling performance, further confirming that the *i*-$Ru_4Cu_1$/CNFs electrocatalyst represents the optimal component in *i*-RuCu/CNFs system for improving the Li-$CO_2$ battery properties. More importantly, with continuously increasing the discharge-charge current density to 1000 mA $g^{-1}$ during cycling process, the Li-$CO_2$ battery based on *i*-$Ru_4Cu_1$/CNFs can still be stably cycled for 120 cycles with negligible decay (Fig. S14).

The rate capability of Li-$CO_2$ batteries was characterized at different current densities ranging from 100 mA $g^{-1}$ to 2000 mA $g^{-1}$. As shown in Fig. 4a, the discharge voltages of the Li-$CO_2$ battery based on *i*-$Ru_4Cu_1$/CNFs are higher than those of Ru/CNFs counterparts over the whole range of current densities. Unexpectedly, the Li-$CO_2$ battery based on *i*-$Ru_4Cu_1$/CNFs delivers remarkably low overpotentials of 1.45 and 1.56 V even at much high current densities of 1000 and 2000 mA $g^{-1}$ (Fig. 4b and c), respectively. The discharge voltage at 2000 mA $g^{-1}$ still reach to 2.62 V, representing the best rate capability ever reported [13, 23, 40]. By contrast, the discharge voltages of Li-$CO_2$ battery based on monometallic Ru/CNFs decrease drastically as current density was increased to 1500 mA $g^{-1}$, which further drop to cutoff voltage of 2 V when current density is 2000 mA $g^{-1}$ (Fig. S15). In addition, the overpotentials of Li-$CO_2$ battery based on *i*-$Ru_4Cu_1$/CNFs are much lower than those of Li-$CO_2$ battery based on Ru/CNFs at all current densities (Fig. 4b). The Li-$CO_2$ battery based on

*i*-$Ru_4Cu_1$/CNFs displays a round-trip efficiency as high as 76 % at current density of 100 mA $g^{-1}$ (Fig. S16), outperforming the corresponding value of 67.5 % for Ru/CNFs counterpart.

The full discharge-charge curves of Li-$CO_2$ batteries were carried out at current density of 300 mA $g^{-1}$. Fig. 4d shows a discharge capacity of 15753 mAh $g^{-1}$ for Li-$CO_2$ battery based on *i*-$Ru_4Cu_1$/CNFs. The discharge-charge cycle is almost completely reversible with a Coulombic efficiency as high as 99.3% (cutoff charge voltage at 4.2 V). Under the same testing conditions, however, the discharge capacity of Li-$CO_2$ battery based on Ru/CNFs is only 8580 mAh $g^{-1}$, much lower than that of Li-$CO_2$ battery based on *i*-$Ru_4Cu_1$/CNFs, with only 34% of the discharged capacity being reversibly charged to the cutoff voltage. Besides, we also investigated the effect of *i*-$Ru_4Cu_1$ mass loading in *i*-$Ru_4Cu_1$/CNFs electrocatalysts on the batteries performance. Interestingly, when the mass loading of *i*-$Ru_4Cu_1$ nanoalloy in *i*-$Ru_4Cu_1$/CNFs electrocatalyst was changed to a lower or higher value (Fig. S17), their discharge capacities are both decreased (Fig. S18) [59], indicating that the *i*-$Ru_4Cu_1$/CNFs with the appropriate metallic mass loading of 38.3% would favorably accelerate the Li-$CO_2$ battery performance .

The above systematically electrochemical studies powerfully demonstrate that the properties of Li-$CO_2$ batteries have been remarkably promoted by using the bimetallic *i*-$Ru_4Cu_1$/CNFs electrocatalysts, which is attributed to the formation of *i*-$Ru_4Cu_1$ solid solution nanoalloys with the favorable electronic structure. Importantly, to more clearly elucidate the alloying effect in *i*-$Ru_4Cu_1$/CNFs for improving the Li-$CO_2$ batteries performance, the *s*-$Ru_4$-$Cu_1$/CNFs electrocatalysts that Ru and Cu nanoparticles separately dispersed on CNFs with the separated phase were further prepared in this work (Fig. S19). As shown in Fig. S20, it is noted that the Li-$CO_2$ battery based on *i*-$Ru_4Cu_1$/CNFs electrocatalyst displays much lower charge-discharge overpotentials than that of Li-$CO_2$ battery based on *s*-$Ru_4$-$Cu_1$/CNFs electrocatalyst at all current densities ranging from 100 to 2000 mA $g^{-1}$, confirming that the *i*-

$Ru_4Cu_1$/CNFs with well-defined solid solution phase could further promote the kinetics of discharge and charge processes for enhancing Li-$CO_2$ batteries performance relative to that of *s*-$Ru_4$-$Cu_1$/CNFs with separated Ru and Cu nanoparticles dispersion. The main reason can be rationally explained that the *i*-$Ru_4Cu_1$/CNFs electrocatalysts with solid solution phase remarkably facilitate the charge transfer between the two different atoms owing to the intimate interactions among these heteroatoms in a solid solution phase compared to that electrocatalysts with separated nanoparticles dispersion. Eventually, the electronic structure of such bimetallic *i*-$Ru_4Cu_1$/CNFs nanoalloys are precisely modified at the atomic level for well tuning the electrochemical properties [50, 60, 61].

*3.3 Analysis of i-$Ru_4Cu_1$/CNFs cathode electrode after discharge-charge processes*

To investigate the discharge products and reversibility of Li-$CO_2$ battery based on *i*-$Ru_4Cu_1$/CNFs, systematical characterizations were further carried out. Fig. 5a presents the XRD patterns of *i*-$Ru_4Cu_1$/CNFs cathodes after full discharge and charge. The obvious diffraction peaks ascribed to $Li_2CO_3$ were observed on discharged *i*-$Ru_4Cu_1$/CNFs electrode, indicating the formation of $Li_2CO_3$ discharge products [13]. After recharging such Li-$CO_2$ battery, the diffraction peaks of $Li_2CO_3$ disappear, uncovering the highly reversible formation and decomposition of crystalline $Li_2CO_3$ promoted by the *i*-$Ru_4Cu_1$/CNFs during discharge-charge processes, which is in accordance with its high Coulombic efficiency. The XPS spectrum of C 1s for discharged *i*-$Ru_4Cu_1$/CNFs electrode shows a new peak at 289.9 eV with much strong intensity, which is assigned to $Li_2CO_3$ (Fig. 5b) [62, 63]. Moreover, the peak at 280.16 eV in terms of Ru 3*d* disappears on such discharged *i*-$Ru_4Cu_1$/CNFs electrode owing to the deposition of discharge products on electrode surface. Intriguingly, after recharging, the XPS peak associated with $Li_2CO_3$ is nearly eliminated with a much faint signal, while the peak representing Ru 3*d* reappears (Fig. 5c), which confirms that $Li_2CO_3$ can be almost reversibly decomposed, allowing the release of $CO_2$ and storing electricity again. Similarly,

the Fourier transform infrared spectra (FTIR) of fully discharged and charged *i*-$Ru_4Cu_1$/CNFs electrodes also show the reversible generation and vanishment of $Li_2CO_3$ during the discharge and charge processes (Fig. S21), further corroborating the results of XRD and XPS analysis [9, 13]. In addition, the XRD and XPS spectra of fully discharged Ru/CNFs and Cu/CNFs cathode electrodes also display the formation of $Li_2CO_3$ products (Fig. S22 and Fig. S23). However, the peaks intensities of XRD and XPS corresponding to the $Li_2CO_3$ are merely slightly decreased for both the fully charged Ru/CNFs and Cu /CNFs cathode electrodes, indicating the limited capability of Ru/CNFs and Cu /CNFs electrocatalysts for effectively decomposing $Li_2CO_3$, which is consistent with their low Coulombic efficiency (Fig. 4d and Fig. S22).

The corresponding morphology changes of *i*-$Ru_4Cu_1$/CNFs electrodes after full discharge and charge were further examined by SEM and TEM. As shown in Fig. 5d and 5f, the discharged *i*-$Ru_4Cu_1$/CNFs electrode surface is totally covered by $Li_2CO_3$. We can deduced that the alloyed *i*-$Ru_4Cu_1$ nanoparticles with the downshifted d-band center facilitate generation and dispersion of $Li_2CO_3$. With increasing discharge depth, the discharge products gradually extend along CNFs surface and eventually cover whole electrode as well as *i*-$Ru_4Cu_1$ nanoparticles. Massive $Li_2CO_3$ would block contact between active sites and reactants, being the chief reason for degradation of battery performance. Notably, it can be seen from Fig. 5e and 5g that the $Li_2CO_3$ products fully disappear after recharging under the help of high-performance *i*-$Ru_4Cu_1$/CNFs, and the morphology of *i*-$Ru_4Cu_1$/CNFs electrode returns back to initial state, preparing for next discharge-charge cycle.

As mentioned in previous researches [9, 12], the reaction mechanism of Li-$CO_2$ batteries is proposed to be the reversible reaction of $4Li + 3CO_2 \leftrightarrow 2Li_2CO_3 + C$. The $Li_2CO_3$ and C species are co-produced during the discharge process. While, during the charge process, only $CO_2$ gas is emitted through the reaction between $Li_2CO_3$ and C. Therefore, to well confirm the $CO_2$ gas emission and examine the discharge products during the cycling process in Li-$CO_2$

batteries, we have systematically carried out the gas chromatography (GC) and Raman measurements by using the carbon-free *i*-$Ru_4Cu_1$ nanomaterials in the customized Swagelok-type Li-$CO_2$ batteries (Fig. S24). As shown in Fig. 6a, the Li-$CO_2$ battery was firstly discharged to a capacity of 5000 mAh $g^{-1}$ at the current density of 300 mA $g^{-1}$ in the pure $CO_2$ gas. Subsequently, after introducing pure Ar gas into such discharged battery to completely eliminate the residual $CO_2$, such Li-$CO_2$ battery was recharged to 5000 mAh $g^{-1}$ for detecting the gas emission during the charge process [29, 64]. Accordingly, three different points (A, B and C) were sequentially taken from the charge process in Fig. 6a to monitor the gas emission by the gas chromatography (GC) instrument. It can be clearly seen that only $CO_2$ gas is detected over the charge process (Fig. 6b). Furthermore, the Raman spectroscopy of discharged carbon-free electrode clearly demonstrates the formation of $Li_2CO_3$ and C products. The peak at 1089 $cm^{-1}$ is ascribed to be $Li_2CO_3$, and the peaks emerging around 1348 $cm^{-1}$ and 1581 $cm^{-1}$ can be identified to be the D and G bands of the produced carbon species after discharge [12, 25]. Intriguingly, after charging such Li-$CO_2$ battery, the characteristic peaks of $Li_2CO_3$ and C disappear, indicating that the $Li_2CO_3$ and C species can be simultaneously decomposed during the charge process. Therefore, based on above comprehensive and fundamental characterizations of GC and Raman spectra, it can be evidently confirmed that the $Li_2CO_3$ and C species are the main discharge products in Li-$CO_2$ batteries, and such $Li_2CO_3$ and C species can be reversibly decomposed to release the only gas of $CO_2$ over the charge process. As a result, the reaction mechanism of Li-$CO_2$ batteries based on *i*-$Ru_4Cu_1$ electrocatalysts is identified to be the reversible reaction of $4Li + 3CO_2 \leftrightarrow 2Li_2CO_3 + C$, which is in line with previous reports [9, 12]. Generally, for the practical Li-$CO_2$ batteries, the carbon nanomaterials, such as Ketjen black [12] and CNFs [15], are commonly employed as the substrates for dispersing the active metal nanoparticles and improving the conductivity. It is a possibility that the $Li_2CO_3$ may selectively react with the CNFs substrates during the charge process, which may be a potential factor for the

degradation of batteries performance. However, it is difficult to distinguish the produced carbon through the reaction of $4Li + 3CO_2 \leftrightarrow 2Li_2CO_3 + C$ from the carbon substrates in the practical Li-$CO_2$ batteris, and currently, the specific reaction mechanism between C and $Li_2CO_3$ is complex and is still unclear. Hence, in the future, more efforts should be devoted on such fundamental investigations to clearly probe the corresponding reaction mechanism.

## Conclusions

In summary, we for the first time report the intermixed bimetallic RuCu nanoalloys that uniformly dispersed on CNFs (*i*-$Ru_4Cu_1$/CNFs) as high-performance cathode electrocatalysts for highly reversible Li-$CO_2$ batteries. Owing to the optimized compositional and electronic effects, the *i*-$Ru_4Cu_1$/CNFs could effectively facilitate the formation and decomposition of $Li_2CO_3$ products during discharge and charge processes, showing exceptional electrocatalytic performance for Li-$CO_2$ batteries. The Li-$CO_2$ batteries based on *i*-$Ru_4Cu_1$/CNFs cathodes exhibit ultra-low overpotentials and can be steadily cycled for over 110 cycles at 500 mA $g^{-1}$ with a fixed capacity of 1000 mAh $g^{-1}$. Moreover, they show the record-high rate capability. These findings reveal that *i*-$Ru_4Cu_1$/CNFs is highly active and stable for Li-$CO_2$ battery performance, much superior to most reported electrocatalysts, which also provides novel view for developing more advanced cathodes in Li-$CO_2$ and other metal-air batteries.

## Acknowledgments

This work was supported by the National Natural Science Foundation of China (grant nos. 51874243, 51271148 and 50971100), the Research Fund of State Key Laboratory of Solidification Processing in China (grant no. 150-ZH-2016), the Aeronautic Science Foundation Program of China (grant no.2012ZF53073), the Project of Transformation of Scientific and Technological Achievements of NWPU (grant no. 19-2017), and the Open Fund of State Key Laboratory of Advanced Technology for Materials Synthesis and

Processing (Wuhan University of Technology grant no. 2018-KF-18). We would like to thank the Analytical & Testing Center of Northwestern Polytechnical University for TEM and SEM characterizations.

## References

[1] W.-H. Wang, Y. Himeda, J.T. Muckerman, G.F. Manbeck, E. Fujita, $CO_2$ Hydrogenation to Formate and Methanol as an Alternative to Photo- and Electrochemical $CO_2$ Reduction, Chem. Rev., 115 (2015) 12936-12973.

[2] F. Marques Mota, D.H. Kim, From $CO_2$ methanation to ambitious long-chain hydrocarbons: alternative fuels paving the path to sustainability, Chem. Soc. Rev., 48 (2019) 205-259.

[3] J. Xie, X. Wang, J. Lv, Y. Huang, M. Wu, Y. Wang, J. Yao, Reversible Aqueous Zinc–$CO_2$ Batteries Based on $CO_2$–HCOOH Interconversion, Angew. Chem., 130 (2018) 17242-17247.

[4] M. Aresta, A. Dibenedetto, A. Angelini, Catalysis for the Valorization of Exhaust Carbon: from CO2 to Chemicals, Materials, and Fuels. Technological Use of $CO_2$, Chem. Rev., 114 (2014) 1709-1742.

[5] Y. Kou, Y. Nabetani, D. Masui, T. Shimada, S. Takagi, H. Tachibana, H. Inoue, Direct Detection of Key Reaction Intermediates in Photochemical $CO_2$ Reduction Sensitized by a Rhenium Bipyridine Complex, J. Am. Chem. Soc., 136 (2014) 6021-6030.

[6] W. Ma, X. Liu, C. Li, H. Yin, W. Xi, R. Liu, G. He, X. Zhao, J. Luo, Y. Ding, Rechargeable Al–$CO_2$ Batteries for Reversible Utilization of $CO_2$, Adv. Mater., 30 (2018) 1801152.

[7] L. Fan, Z. Xia, M. Xu, Y. Lu, Z. Li, 1D $SnO_2$ with Wire-in-Tube Architectures for Highly Selective Electrochemical Reduction of $CO_2$ to C1 Products, Adv. Funct. Mater., 28 (2018) 1706289.

[8] Z. Xie, X. Zhang, Z. Zhang, Z. Zhou, Metal–$CO_2$ Batteries on the Road: $CO_2$ from Contamination Gas to Energy Source, Adv. Mater., 29 (2017) 1605891.

[9] Y. Qiao, J. Yi, S. Wu, Y. Liu, S. Yang, P. He, H. Zhou, Li-$CO_2$ Electrochemistry: A New Strategy for $CO_2$ Fixation and Energy Storage, Joule, 1 (2017) 359-370.

[10] S. Xu, S.K. Das, L.A. Archer, The Li–$CO_2$ battery: a novel method for $CO_2$ capture and utilization, RSC Adv., 3 (2013) 6656-6660.

[11] X. Li, S. Yang, N. Feng, P. He, H. Zhou, Progress in research on Li–$CO_2$ batteries: Mechanism, catalyst and performance, Chinese Journal of Catalysis, 37 (2016) 1016-1024.

[12] S. Yang, Y. Qiao, P. He, Y. Liu, Z. Cheng, J.-j. Zhu, H. Zhou, A reversible lithium–$CO_2$ battery with Ru nanoparticles as a cathode catalyst, Energy Environ. Sci, 10 (2017) 972-978.

[13] L. Qie, Y. Lin, J.W. Connell, J. Xu, L. Dai, Highly Rechargeable Lithium-$CO_2$ Batteries with a Boron- and Nitrogen-Codoped Holey-Graphene Cathode, Angew. Chem. Int. Ed., 56 (2017) 6970-6974.

[14] Y. Jin, C. Hu, Q. Dai, Y. Xiao, Y. Lin, J.W. Connell, F. Chen, L. Dai, High-Performance Li-$CO_2$ Batteries Based on Metal-Free Carbon Quantum Dot/Holey Graphene Composite Catalysts, Adv. Funct. Mater., 28 (2018) 1804630.

[15] C. Wang, Q. Zhang, X. Zhang, X.-G. Wang, Z. Xie, Z. Zhou, Fabricating Ir/C Nanofiber Networks as Free-Standing Air Cathodes for Rechargeable Li-$CO_2$ Batteries, Small, 14 (2018) 1800641.

[16] Y. Mao, C. Tang, Z. Tang, J. Xie, Z. Chen, J. Tu, G. Cao, X. Zhao, Long-life Li–$CO_2$ cells with ultrafine $IrO_2$-decorated few-layered δ-$MnO_2$ enabling amorphous $Li_2CO_3$ growth, Energy Storage Mater., 18 (2019) 405-413.

[17] Y. Qiao, J. Yi, S. Guo, Y. Sun, S. Wu, X. Liu, S. Yang, P. He, H. Zhou, $Li_2CO_3$-free Li–$O_2$/$CO_2$ battery with peroxide discharge product, Energy Environ. Sci., 11 (2018) 1211-1217.

[18] J. Chen, K. Zou, P. Ding, J. Deng, C. Zha, Y. Hu, X. Zhao, J. Wu, J. Fan, Y. Li, Conjugated Cobalt Polyphthalocyanine as the Elastic and Reprocessable Catalyst for Flexible Li–$CO_2$ Batteries, Adv. Mater., 31 (2019) 1805484.

[19] K. Takechi, T. Shiga, T. Asaoka, A Li–$O_2$/$CO_2$ battery, Chem. Commun., 47 (2011) 3463-3465.

[20] Z. Zhang, Q. Zhang, Y. Chen, J. Bao, X. Zhou, Z. Xie, J. Wei, Z. Zhou, The First Introduction of Graphene to Rechargeable Li–$CO_2$ Batteries, Angew. Chem. Int. Ed., 54 (2015) 6550-6553.

[21] Y. Xing, Y. Yang, D. Li, M. Luo, N. Chen, Y. Ye, J. Qian, L. Li, D. Yang, F. Wu, R. Chen, S. Guo, Crumpled Ir Nanosheets Fully Covered on Porous Carbon Nanofibers for Long-Life Rechargeable Lithium–$CO_2$ Batteries, Adv. Mater., 30 (2018) 1803124.

[22] Z. Zhang, X.-G. Wang, X. Zhang, Z. Xie, Y.-N. Chen, L. Ma, Z. Peng, Z. Zhou, Verifying the Rechargeability of Li-$CO_2$ Batteries on Working Cathodes of Ni Nanoparticles Highly Dispersed on N-Doped Graphene, Adv. Sci., 5 (2018) 1700567.

[23] Y. Qiao, Y. Liu, C. Chen, H. Xie, Y. Yao, S. He, W. Ping, B. Liu, L. Hu, 3D-Printed Graphene Oxide Framework with Thermal Shock Synthesized Nanoparticles for Li-$CO_2$ Batteries, Adv. Funct. Mater., 28 (2018) 1805899.

[24] Z. Zhang, Z. Zhang, P. Liu, Y. Xie, K. Cao, Z. Zhou, Identification of cathode stability in Li–$CO_2$ batteries with Cu nanoparticles highly dispersed on N-doped graphene, J. Mater. Chem. A, 6 (2018) 3218-3223.

[25] W. Ma, S. Lu, X. Lei, X. Liu, Y. Ding, Porous $Mn_2O_3$ cathode for highly durable Li–$CO_2$ batteries, J. Mater. Chem. A, 6 (2018) 20829-20835.

[26] R. Pipes, A. Bhargav, A. Manthiram, Nanostructured Anatase Titania as a Cathode Catalyst for Li–$CO_2$ Batteries, ACS Applied Mater. Interfaces, 10 (2018) 37119-37124.

[27] Y. Hou, J. Wang, L. Liu, Y. Liu, S. Chou, D. Shi, H. Liu, Y. Wu, W. Zhang, J. Chen, $Mo_2C$/CNT: An Efficient Catalyst for Rechargeable Li–$CO_2$ Batteries, Adv. Funct. Mater., 27 (2017) 1700564.

[28] J. Zhou, X. Li, C. Yang, Y. Li, K. Guo, J. Cheng, D. Yuan, C. Song, J. Lu, B. Wang, A Quasi-Solid-State Flexible Fiber-Shaped Li–$CO_2$ Battery with Low Overpotential and High Energy Efficiency, Adv. Mater., 31 (2019) 1804439.

[29] J. Li, H. Zhao, H. Qi, X. Sun, X. Song, Z. Guo, A.G. Tamirat, J. Liu, L. Wang, S. Feng, Drawing a Pencil-Trace Cathode for a High-Performance Polymer-Based Li–$CO_2$ Battery with Redox Mediator, Adv. Funct. Mater., 29 (2019) 1806863.

[30] X. Zhang, Q. Zhang, Z. Zhang, Y. Chen, Z. Xie, J. Wei, Z. Zhou, Rechargeable Li–CO2 batteries with carbon nanotubes as air cathodes, Chem. Commun., 51 (2015) 14636-14639.

[31] H. Zhao, D. Li, H. Li, A.G. Tamirat, X. Song, Z. Zhang, Y. Wang, Z. Guo, L. Wang, S. Feng, Ru nanosheet catalyst supported by three-dimensional nickel foam as a binder-free cathode for Li–$CO_2$ batteries, Electrochimica Acta, 299 (2019) 592-599.

[32] S.-M. Xu, Z.-C. Ren, X. Liu, X. Liang, K.-X. Wang, J.-S. Chen, Carbonate decomposition: Low-overpotential Li-$CO_2$ battery based on interlayer-confined monodisperse catalyst, Energy Storage Mater., 15 (2018) 291-298.

[33] J. Gu, Y.-W. Zhang, F. Tao, Shape control of bimetallic nanocatalysts through well-designed colloidal chemistry approaches, Chem. Soc. Rev., 41 (2012) 8050-8065.

[34] K.D. Gilroy, A. Ruditskiy, H.-C. Peng, D. Qin, Y. Xia, Bimetallic Nanocrystals: Syntheses, Properties, and Applications, Chem. Rev., 116 (2016) 10414-10472.

[35] V.R. Stamenkovic, B.S. Mun, M. Arenz, K.J.J. Mayrhofer, C.A. Lucas, G. Wang, P.N. Ross, N.M. Markovic, Trends in electrocatalysis on extended and nanoscale Pt-bimetallic alloy surfaces, Nat. Mater., 6 (2007) 241.

[36] H. He, X. Xu, H. Wu, Y. Jin, Enzymatic Plasmonic Engineering of Ag/Au Bimetallic Nanoshells and Their Use for Sensitive Optical Glucose Sensing, Adv. Mater., 24 (2012) 1736-1740.

[37] J. Jung, K. Song, Y. Bae, S.-I. Choi, M. Park, E. Cho, K. Kang, Y.-M. Kang, Achieving outstanding $Li^+$-ORR and -OER activities via edge- and corner-embedded bimetallic nanocubes for rechargeable Li–$O_2$ batteries, Nano Energy, 18 (2015) 71-80.

[38] Y.-C. Lu, Z. Xu, H.A. Gasteiger, S. Chen, K. Hamad-Schifferli, Y. Shao-Horn, Platinum−Gold Nanoparticles: A Highly Active Bifunctional Electrocatalyst for Rechargeable Lithium−Air Batteries, J. Am. Chem. Soc., 132 (2010) 12170-12171.

[39] R. Choi, J. Jung, G. Kim, K. Song, Y.-I. Kim, S.C. Jung, Y.-K. Han, H. Song, Y.-M. Kang, Ultra-low overpotential and high rate capability in Li–$O_2$ batteries through surface atom arrangement of PdCu nanocatalysts, Energy Environ. Sci., 7 (2014) 1362-1368.

[40] Z. Zhang, C. Yang, S. Wu, A. Wang, L. Zhao, D. Zhai, B. Ren, K. Cao, Z. Zhou, Exploiting Synergistic Effect by Integrating Ruthenium–Copper Nanoparticles Highly Co-Dispersed on Graphene as Efficient Air Cathodes for Li–$CO_2$ Batteries, Adv. Energy Mater., 9 (2019) 1802805.

[41] J.R. Kitchin, J.K. Nørskov, M.A. Barteau, J.G. Chen, Role of Strain and Ligand Effects in the Modification of the Electronic and Chemical Properties of Bimetallic Surfaces, Phy. Rev. Lett., 93 (2004) 156801.

[42] X. Wang, Y. Zhu, A. Vasileff, Y. Jiao, S. Chen, L. Song, B. Zheng, Y. Zheng, S.-Z. Qiao, Strain Effect in Bimetallic Electrocatalysts in the Hydrogen Evolution Reaction, ACS Energy Lett., 3 (2018) 1198-1204.

[43] J. Shui, M. Wang, F. Du, L. Dai, N-doped carbon nanomaterials are durable catalysts for oxygen reduction reaction in acidic fuel cells, Sci. Adv., 1 (2015) e1400129.

[44] Y. Liang, H. Wang, P. Diao, W. Chang, G. Hong, Y. Li, M. Gong, L. Xie, J. Zhou, J. Wang, T.Z. Regier, F. Wei, H. Dai, Oxygen Reduction Electrocatalyst Based on Strongly

Coupled Cobalt Oxide Nanocrystals and Carbon Nanotubes, J. Am. Chem. Soc., 134 (2012) 15849-15857.

[45] J. Mahmood, F. Li, S.-M. Jung, M.S. Okyay, I. Ahmad, S.-J. Kim, N. Park, H.Y. Jeong, J.-B. Baek, An efficient and pH-universal ruthenium-based catalyst for the hydrogen evolution reaction, Nat. Nanotech., 12 (2017) 441.

[46] W. Li, Y. Liu, M. Wu, X. Feng, S.A.T. Redfern, Y. Shang, X. Yong, T. Feng, K. Wu, Z. Liu, B. Li, Z. Chen, J.S. Tse, S. Lu, B. Yang, Carbon-Quantum-Dots-Loaded Ruthenium Nanoparticles as an Efficient Electrocatalyst for Hydrogen Production in Alkaline Media, Adv. Mater., 30 (2018) 1800676.

[47] Y. Chen, Z. Yu, Z. Chen, R. Shen, Y. Wang, X. Cao, Q. Peng, Y. Li, Controlled one-pot synthesis of RuCu nanocages and Cu@Ru nanocrystals for the regioselective hydrogenation of quinoline, Nano Research, 9 (2016) 2632-2640.

[48] J. Wang, F. Chen, Y. Jin, R.L. Johnston, Gold–Copper Aerogels with Intriguing Surface Electronic Modulation as Highly Active and Stable Electrocatalysts for Oxygen Reduction and Borohydride Oxidation, ChemSusChem, 11 (2018) 1354-1364.

[49] Y. Yao, Z. Huang, P. Xie, S.D. Lacey, R.J. Jacob, H. Xie, F. Chen, A. Nie, T. Pu, M. Rehwoldt, D. Yu, M.R. Zachariah, C. Wang, R. Shahbazian-Yassar, J. Li, L. Hu, Carbothermal shock synthesis of high-entropy-alloy nanoparticles, Science, 359 (2018) 1489-1494.

[50] B. Huang, H. Kobayashi, T. Yamamoto, S. Matsumura, Y. Nishida, K. Sato, K. Nagaoka, S. Kawaguchi, Y. Kubota, H. Kitagawa, Solid-Solution Alloying of Immiscible Ru and Cu with Enhanced CO Oxidation Activity, J. Am. Chem. Soc., 139 (2017) 4643-4646.

[51] Y. Liu, S. Liu, Y. Wang, Q. Zhang, L. Gu, S. Zhao, D. Xu, Y. Li, J. Bao, Z. Dai, Ru Modulation Effects in the Synthesis of Unique Rod-like Ni@$Ni_2P$–Ru Heterostructures and Their Remarkable Electrocatalytic Hydrogen Evolution Performance, J. Am. Chem. Soc., 140 (2018) 2731-2734.

[52] L. Wang, Q. Zhou, Z. Pu, Q. Zhang, X. Mu, H. Jing, S. Liu, C. Chen, S. Mu, Surface reconstruction engineering of cobalt phosphides by Ru inducement to form hollow Ru-$RuP_x$-$Co_xP$ pre-electrocatalysts with accelerated oxygen evolution reaction, Nano Energy, 53 (2018) 270-276.

[53] S. Nong, W. Dong, J. Yin, B. Dong, Y. Lu, X. Yuan, X. Wang, K. Bu, M. Chen, S. Jiang, L.-M. Liu, M. Sui, F. Huang, Well-Dispersed Ruthenium in Mesoporous Crystal $TiO_2$ as an Advanced Electrocatalyst for Hydrogen Evolution Reaction, J. Am. Chem. Soc., 140 (2018) 5719-5727.

[54] F. Wang, K. Kusada, D. Wu, T. Yamamoto, T. Toriyama, S. Matsumura, Y. Nanba, M. Koyama, H. Kitagawa, Solid-Solution Alloy Nanoparticles of the Immiscible Iridium–Copper System with a Wide Composition Range for Enhanced Electrocatalytic Applications, Angew. Chem. Int. Ed., 57 (2018) 4505-4509.

[55] Y. Jin, F. Chen, Facile preparation of Ag-Cu bifunctional electrocatalysts for zinc-air batteries, Electrochimica Acta, 158 (2015) 437-445.

[56] M.-M. Shi, D. Bao, S.-J. Li, B.-R. Wulan, J.-M. Yan, Q. Jiang, Anchoring PdCu Amorphous Nanocluster on Graphene for Electrochemical Reduction of $N_2$ to $NH_3$ under Ambient Conditions in Aqueous Solution, Adv. Energy Mater., 8 (2018) 1800124.

[57] B. Huang, H. Kobayashi, T. Yamamoto, T. Toriyama, S. Matsumura, Y. Nishida, K. Sato, K. Nagaoka, M. Haneda, W. Xie, Y. Nanba, M. Koyama, F. Wang, S. Kawaguchi, Y. Kubota, H. Kitagawa, A CO Adsorption Site Change Induced by Copper Substitution in a Ruthenium Catalyst for Enhanced CO Oxidation Activity, Angew. Chem., 131 (2019) 2252-2257.

[58] S. Song, W. Xu, J. Zheng, L. Luo, M.H. Engelhard, M.E. Bowden, B. Liu, C.-M. Wang, J.-G. Zhang, Complete Decomposition of $Li_2CO_3$ in Li–$O_2$ Batteries Using Ir/$B_4C$ as Noncarbon-Based Oxygen Electrode, Nano Lett., 17 (2017) 1417-1424.

[59] K. Guo, Y. Li, J. Yang, Z. Zou, X. Xue, X. Li, H. Yang, Nanosized Mn–Ru binary oxides as effective bifunctional cathode electrocatalysts for rechargeable Li–$O_2$ batteries, J. Mater. Chem. A, 2 (2014) 1509-1514.

[60] X.X. Wang, S. Hwang, Y.-T. Pan, K. Chen, Y. He, S. Karakalos, H. Zhang, J.S. Spendelow, D. Su, G. Wu, Ordered $Pt_3Co$ Intermetallic Nanoparticles Derived from Metal–Organic Frameworks for Oxygen Reduction, Nano Lett., 18 (2018) 4163-4171.

[61] Z. Cui, L. Li, A. Manthiram, J.B. Goodenough, Enhanced Cycling Stability of Hybrid Li–Air Batteries Enabled by Ordered $Pd_3Fe$ Intermetallic Electrocatalyst, J. Am. Chem. Soc., 137 (2015) 7278-7281.

[62] Y. Li, J. Zhou, T. Zhang, T. Wang, X. Li, Y. Jia, J. Cheng, Q. Guan, E. Liu, H. Peng, B. Wang, Highly Surface-Wrinkled and N-Doped CNTs Anchored on Metal Wire: A Novel Fiber-Shaped Cathode toward High-Performance Flexible Li–$CO_2$ Batteries, Adv. Funct. Mater., 29 (2019) 1808117.

[63] X. Zhang, C. Wang, H. Li, X.-G. Wang, Y.-N. Chen, Z. Xie, Z. Zhou, High performance Li–$CO_2$ batteries with NiO–CNT cathodes, J. Mater. Chem. A, 6 (2018) 2792-2796.

[64] S. Li, Y. Dong, J. Zhou, Y. Liu, J. Wang, X. Gao, Y. Han, P. Qi, B. Wang, Carbon dioxide in the cage: manganese metal–organic frameworks for high performance $CO_2$ electrodes in Li–$CO_2$ batteries, Energy Environ. Sci., 11 (2018) 1318-1325.

## Figure captions

**Fig. 1**. (a) XRD patterns of Ru/CNFs and *i*-$Ru_4Cu_1$/CNFs. Inset in (a) is the corresponding enlarged image. (b, c) Bright-field TEM image of *i*-$Ru_4Cu_1$/CNFs. (d) HRTEM of *i*-$Ru_4Cu_1$/CNFs derived from the yellow frame in (c). (e) Lattice fringe distance for *i*-$Ru_4Cu_1$ nanoalloy derived from the blue frame in (d). (f) HAADF-STEM image and (g-i) corresponding element mappings. (j) Line-scan of a single *i*-$Ru_4Cu_1$ nanoparticle.

**Fig. 2**. (a) Full XPS survey spectra for Ru/CNFs, *i*-$Ru_4Cu_1$/CNFs and Cu/CNFs. (b) High-resolution XPS spectra of Ru3*p* for Ru/CNFs and *i*-$Ru_4Cu_1$/CNFs. (c) High-resolution XPS spectra of Cu2*p* for *i*-$Ru_4Cu_1$/CNFs and Cu/CNFs. (d) Valence band spectra (VBS) for Ru/CNFs, *i*-$Ru_4Cu_1$/CNFs and Cu/CNFs.

**Fig. 3.** (a) Galvanostatic discharge-charge curves of Li-$CO_2$ batteries based on *i*-$Ru_4Cu_1$/CNFs, Ru/CNFs and CNFs electrocatalysts at current density of 100 mA $g^{-1}$ with cut-off capacity of 1000 mAh $g^{-1}$. (b) Comparison of overpotentials, discharge and charge voltages derived from (a). (c) Galvanostatic discharge-charge curves of Li-$CO_2$, Li-$O_2$ and Li-air batteries based *i*-$Ru_4Cu_1$/CNFs electrocatalysts at current density of 100 mA $g^{-1}$ with cut-off capacity of 1000 mAh $g^{-1}$. (d) Cycling ability of Li-$CO_2$ batteries based on *i*-$Ru_4Cu_1$/CNFs and Ru/CNFs electrocatalysts at current density of 500 mA $g^{-1}$ with cut-off capacity of 1000 mAh $g^{-1}$. (e) Selected discharge-charge curves of Li-$CO_2$ battery based on *i*-$Ru_4Cu_1$/CNFs electrocatalyst. (f) Comparison of time-voltage curves during the whole discharge-charge processes.

**Fig. 4.** (a) Rate capabilities and (b) comparison of overpotentials of Li-$CO_2$ batteries based on *i*-$Ru_4Cu_1$/CNFs and Ru/CNFs electrocatalysts at current densities ranging from 100 mA $g^{-1}$ to 2000 mA $g^{-1}$. (c) Selected discharge-charge curves of Li-$CO_2$ battery based on *i*-$Ru_4Cu_1$/CNFs electrocatalyst at various current densities. (d) Full discharge-charge curves of Li-$CO_2$ batteries based on *i*-$Ru_4Cu_1$/CNFs and Ru/CNFs electrocatalysts at current density of 300 mA $g^{-1}$.

**Fig. 5.** (a) XRD patterns of discharged and charged *i*-$Ru_4Cu_1$/CNFs electrodes in Li-$CO_2$ batteries. High-resolution XPS spectra of (b) discharged and (c) charged *i*-$Ru_4Cu_1$/CNFs electrodes in Li-$CO_2$ batteries. SEM images of (d) discharged and (e) charged *i*-$Ru_4Cu_1$/CNFs electrodes in Li-$CO_2$ batteries. TEM images of (f) discharged and (g) charged *i*-$Ru_4Cu_1$/CNFs electrodes in Li-$CO_2$ batteries.

**Fig. 6.** (a) Galvanostatic discharge-charge profile of Li-$CO_2$ battery based on a carbon-free *i*-$Ru_4Cu_1$ cathode electrode at a current density of 300 mA $g^{-1}$ with cut-off capacity of 5000 mAh $g^{-1}$. (b) the GC curves of selective points during the charge process obtained from (a). (c) The Raman spectra of the discharged and charged carbon-free *i*-$Ru_4Cu_1$ cathode electrodes in the Li-$CO_2$ batteries at a current density of 300 mA $g^{-1}$ with cut-off capacity of 5000 mAh $g^{-1}$.

**Fig. 1**

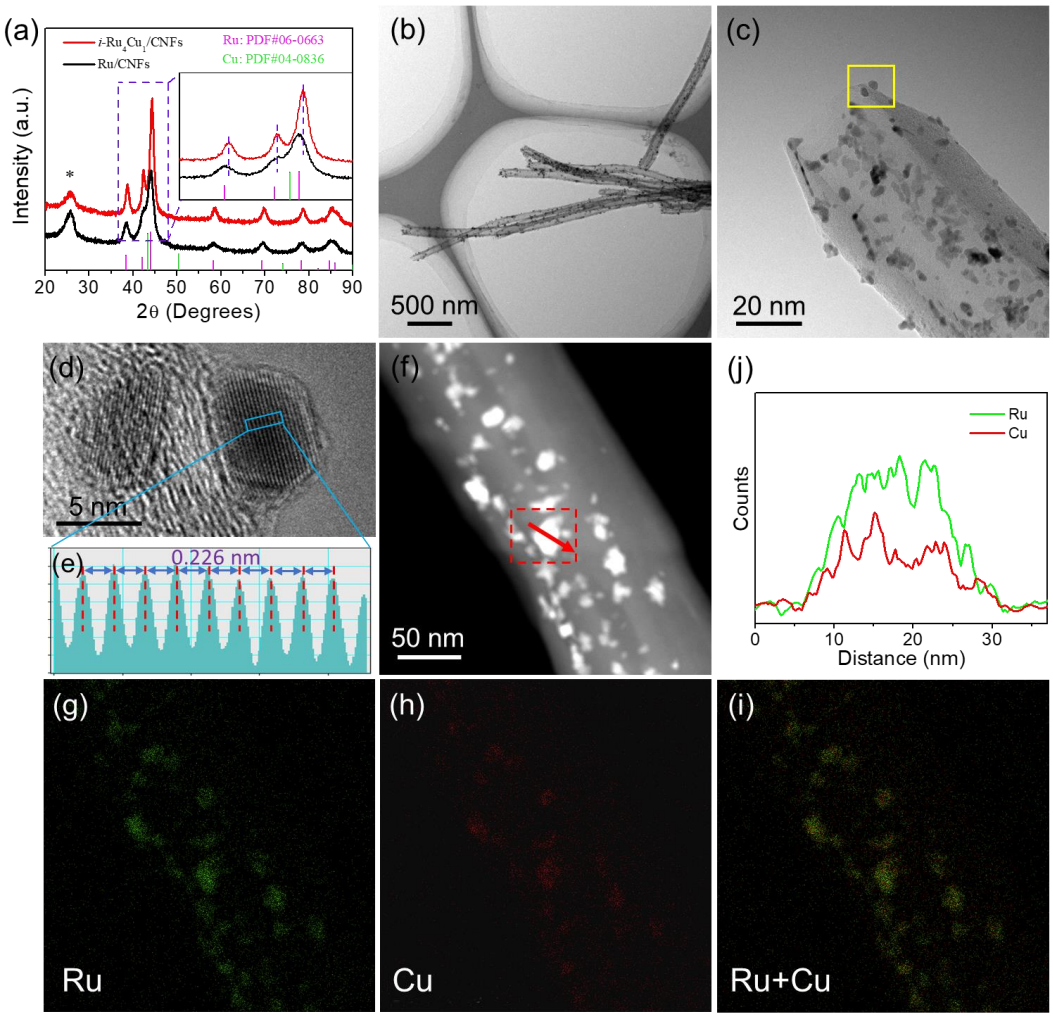
(a)
t-Ru4Cu1/CNFs
Ru/CNFs
Ru: PDF#06-0663
Cu: PDF#04-0836
Intensity (a.u.)
2θ (Degrees)
(b)
500 nm
(c)
20 nm
(d)
5 nm
(e)
0.226 nm
(f)
50 nm
(j)
Ru
Cu
Counts
Distance (nm)
(g)
Ru
(h)
Cu
(i)
Ru+Cu

**Fig. 2**

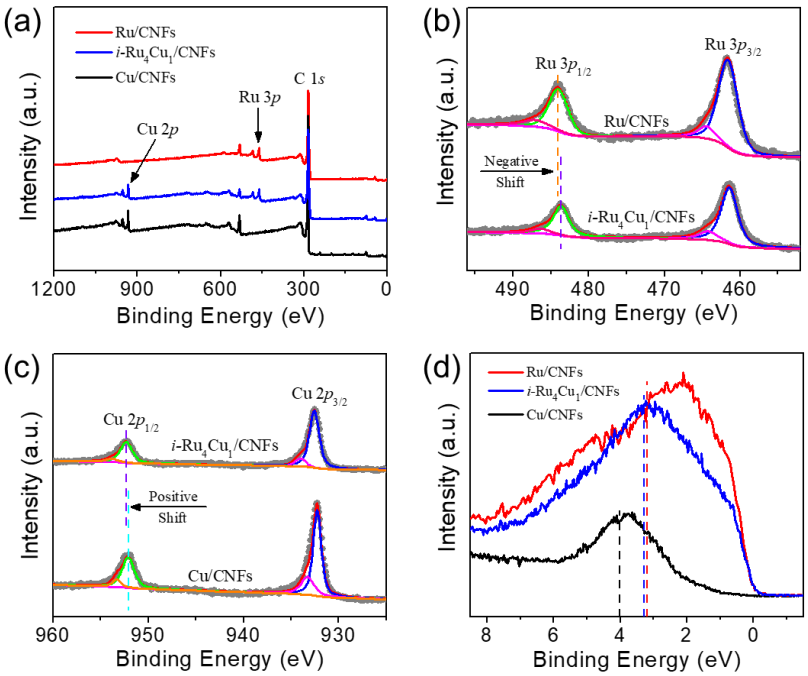
(a)
Ru/CNFs
i-Ru4Cu1/CNFs
Cu/CNFs
C 1s
Ru 3p
Cu 2p
Intensity (a.u.)
1200
900
600
300
0
Binding Energy (eV)
(b)
Ru 3p1/2
Ru 3p3/2
Ru/CNFs
Negative
Shift
i-Ru4Cu1/CNFs
Intensity (a.u.)
490
480
470
460
Binding Energy (eV)
(c)
Cu 2p1/2
Cu 2p3/2
i-Ru4Cu1/CNFs
Positive
Shift
Cu/CNFs
Intensity (a.u.)
960
950
940
930
Binding Energy (eV)
(d)
Ru/CNFs
i-Ru4Cu1/CNFs
Cu/CNFs
Intensity (a.u.)
8
6
4
2
0
Binding Energy (eV)

**Fig. 3**

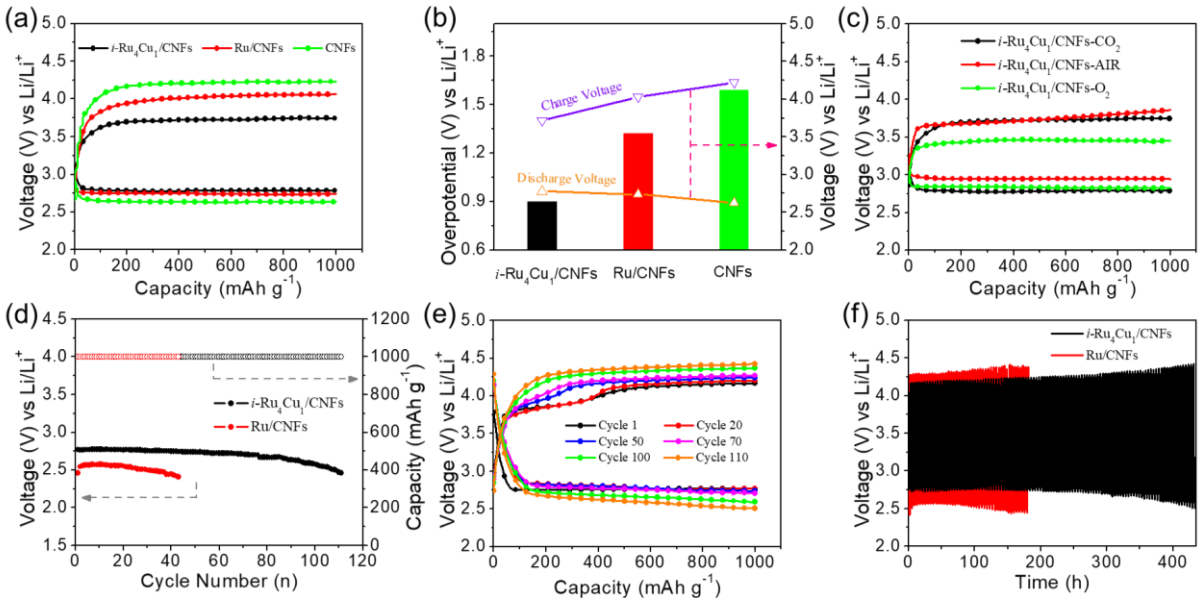
(a)
i-Ru4Cu1/CNFs
Ru/CNFs
CNFs
Voltage (V) vs Li/Li+
Capacity (mAh g-1)
(b)
Charge Voltage
Discharge Voltage
Overpotential (V) vs Li/Li+
i-Ru4Cu1/CNFs
Ru/CNFs
CNFs
(c)
i-Ru4Cu1/CNFs-CO2
i-Ru4Cu1/CNFs-AIR
i-Ru4Cu1/CNFs-O2
Voltage (V) vs Li/Li+
Capacity (mAh g-1)
(d)
i-Ru4Cu1/CNFs
Ru/CNFs
Voltage (V) vs Li/Li+
Capacity (mAh g-1)
Cycle Number (n)
(e)
Cycle 1
Cycle 20
Cycle 50
Cycle 70
Cycle 100
Cycle 110
Voltage (V) vs Li/Li+
Capacity (mAh g-1)
(f)
i-Ru4Cu1/CNFs
Ru/CNFs
Voltage (V) vs Li/Li+
Time (h)

**Fig. 4**

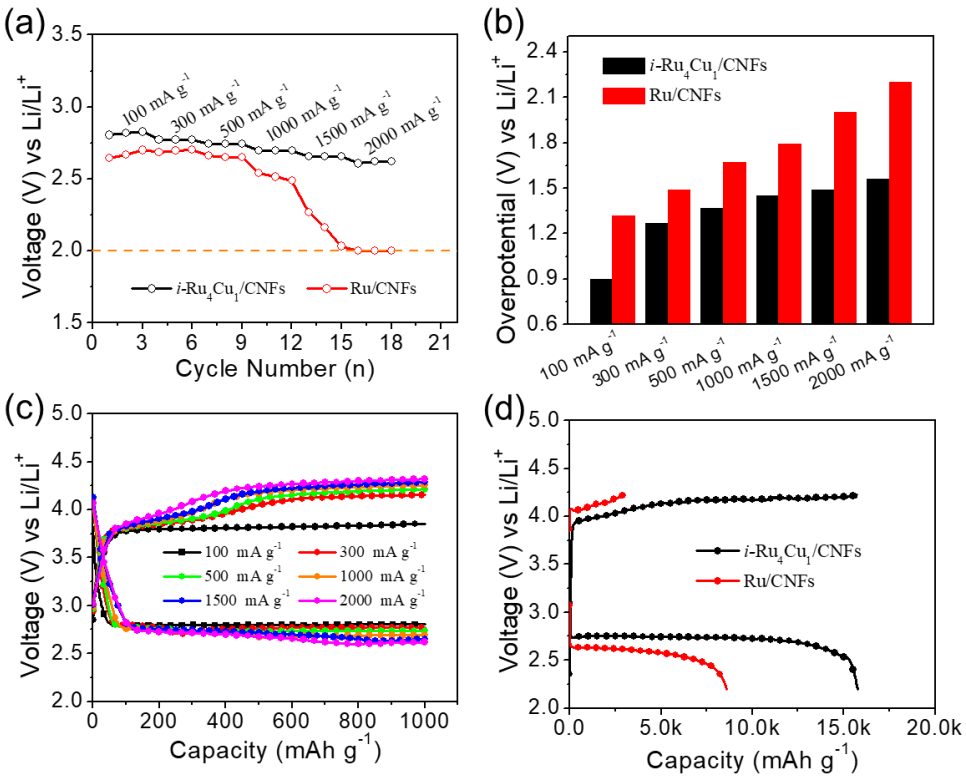
(a)
Voltage (V) vs Li/Li+
Cycle Number (n)
100 mA g-1
300 mA g-1
500 mA g-1
1000 mA g-1
1500 mA g-1
2000 mA g-1
i-Ru4Cu1/CNFs
Ru/CNFs
(b)
Overpotential (V) vs Li/Li+
i-Ru4Cu1/CNFs
Ru/CNFs
100 mA g-1
300 mA g-1
500 mA g-1
1000 mA g-1
1500 mA g-1
2000 mA g-1
(c)
Voltage (V) vs Li/Li+
Capacity (mAh g-1)
100 mA g-1
300 mA g-1
500 mA g-1
1000 mA g-1
1500 mA g-1
2000 mA g-1
(d)
Voltage (V) vs Li/Li+
Capacity (mAh g-1)
i-Ru4Cu1/CNFs
Ru/CNFs

**Fig. 5**

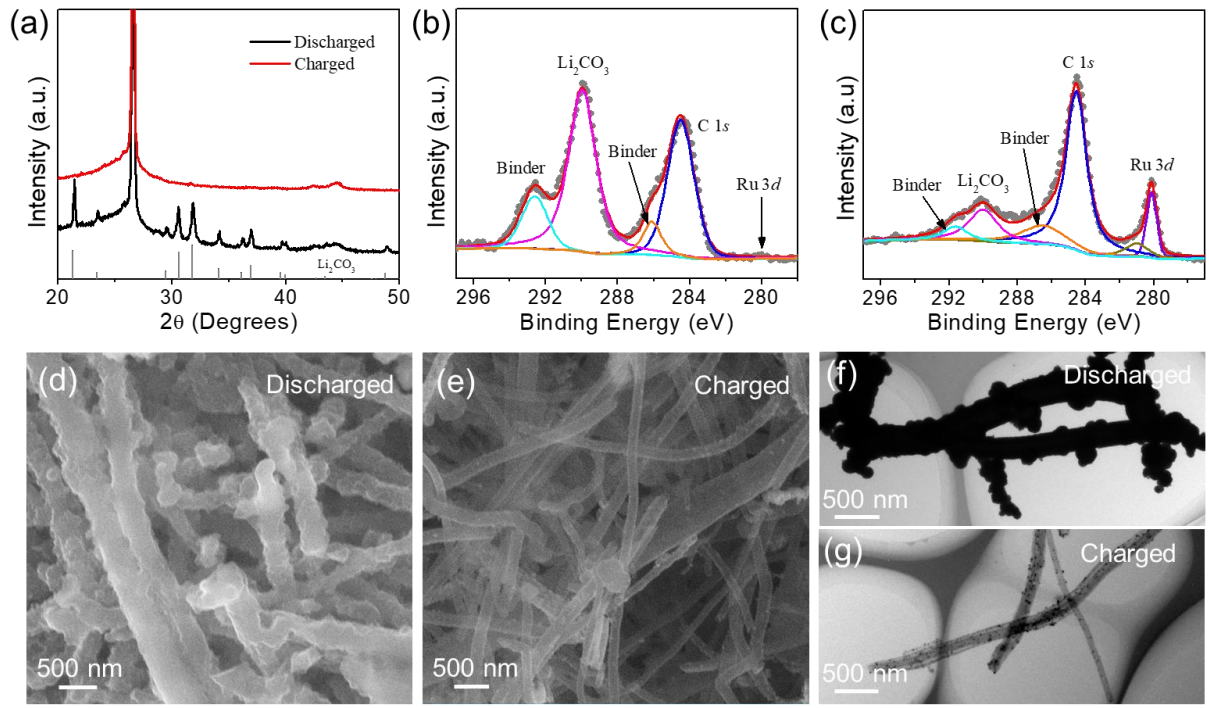
(a)
Discharged
Charged
Intensity (a.u.)
Li2CO3
20
30
40
50
2θ (Degrees)
(b)
Li2CO3
Binder
Binder
C 1s
Ru 3d
Intensity (a.u.)
296
292
288
284
280
Binding Energy (eV)
(c)
C 1s
Binder
Binder
Li2CO3
Ru 3d
Intensity (a.u)
296
292
288
284
280
Binding Energy (eV)
(d)
Discharged
500 nm
(e)
Charged
500 nm
(f)
Discharged
500 nm
(g)
Charged
500 nm

**Fig. 6**

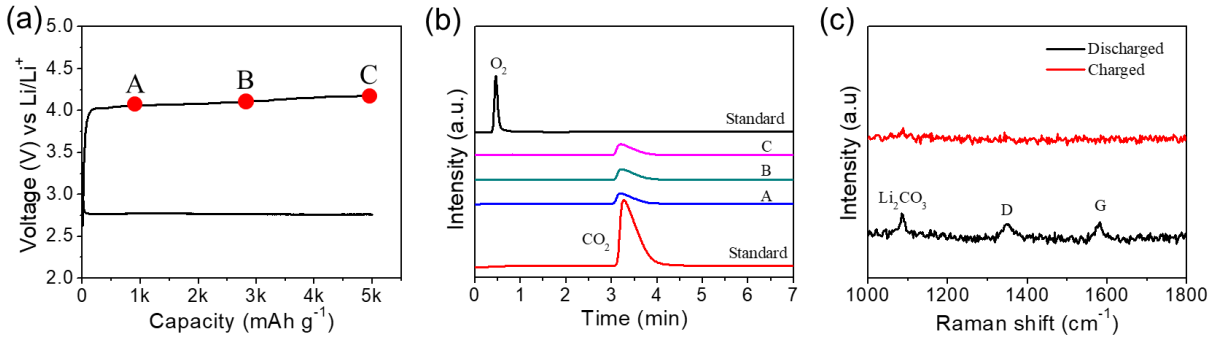
(a)
Voltage (V) vs Li/Li+
Capacity (mAh g-1)
A
B
C
(b)
Intensity (a.u.)
Time (min)
O2
Standard
C
B
A
CO2
Standard
(c)
Intensity (a.u)
Raman shift (cm-1)
Discharged
Charged
Li2CO3
D
G